JACS Au
AN OPEN ACCESS JOURNAL OF THE AMERICAN CHEMICAL SOCIETY

Open Access
This article is licensed under CC-BY-NC-ND 4.0

pubs.acs.org/jacsau
Article

Changes in Active Site Loop Conformation Relate to the Transition toward a Novel Enzymatic Activity

Pauline Jacquet, Raphaël Billot, Amir Shimon, Nathan Hoekstra, Céline Bergonzi, Anthony Jenks, Eric Chabrière, David Daudé,* and Mikael H. Elias*

Cite This: *JACS Au* 2024, 4, 1941−1953
Read Online

ACCESS | Metrics & More | Article Recommendations | Supporting Information

ABSTRACT: Enzymatic promiscuity, the ability of enzymes to catalyze multiple, distinct chemical reactions, has been well documented and is hypothesized to be a major driver of the emergence of new enzymatic functions. Yet, the molecular mechanisms involved in the transition from one activity to another remain debated and elusive. Here, we evaluated the redesign of the active site binding cleft of lactonase *Sso*Pox using structure-based design and combinatorial libraries. We created variants with largely improved catalytic abilities against phosphotriesters, the best ones being >1000-fold better compared to the wild-type enzyme. The observed shifts in activity specificity are large, and some variants completely lost their initial activity. The selected combinations of mutations have considerably reshaped the active site cavity via side chain changes but mostly through large rearrangements of the active site loops and changes to their conformations, as revealed by a suite of crystal structures. This suggests that a specific active site loop configuration is critical to the lactonase activity. Interestingly, analysis of high-resolution structures hints at the potential role of conformational sampling and its directionality in defining the enzyme activity profile.

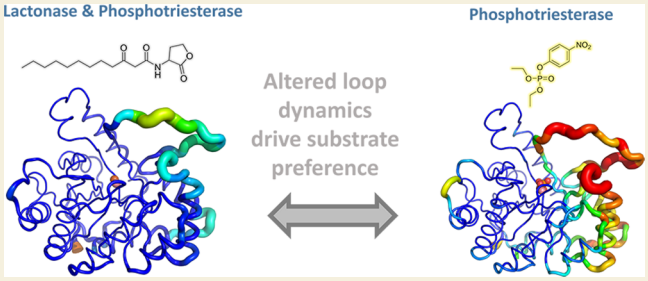

KEYWORDS: *lactonase, phosphotriesterase, enzymatic promiscuity, conformational dynamics, conformational directionality*

1. INTRODUCTION

Over the past years, it has become evident that enzymes may accept more than one substrate or catalyze more than one specific reaction, and much attention has been paid to investigating the role of enzyme promiscuity in the emergence of new catalytic functions.[1−3] Promiscuous activities may confer adaptability and could constitute an advantage under selection pressure.[4,5] The transition between phenotypes has been shown to be relatively close in the genotype space, the acquisition of new functions being gradual and smooth in the course of evolution.[6,7] Catalytic promiscuity may therefore be used as a starting point for directed evolution strategies.[8−10]

The hypothesized recent emergence of phosphotriesterase (PTE) enzymes is a striking example of the role of enzyme promiscuity in selective adaptation. Indeed, the wide use of organophosphorus (OP) insecticides since the 1950s for agricultural purposes may have led to the emergence of highly efficient OP-degrading enzymes for the mobilization of the poorly available phosphate.[11] Several highly proficient bacterial PTEs appear to have emerged from a promiscuous lactonase template belonging to the phosphotriesterase-like lactonase (PLL) family.[11,12] PLLs are enzymes that are naturally able to catalyze the hydrolysis of lactones, especially acyl-homoserine lactones involved in bacterial communication referred to as quorum sensing.[11,13] Besides their lactonase activity, most PLLs show a promiscuous activity toward phosphotriesters, which may rely on the similarity of the tetrahedral intermediate involved in their respective reactions.[14] PLL and PTE share a $(\beta/\alpha)_8$ fold with highly mobile loops that contribute to broadening their promiscuity to other substrates such as aryl-esters.[15] Bacterial PTEs, although naturally efficient for the degradation of OP insecticides, have been further engineered in vitro for the development of biocatalysts close to catalytic perfection for decontaminating insecticides or chemical warfare agents.[16−23] These variants may find application in bioremediation of agricultural contaminations or for prophylaxis protection against OP poisoning.[24,25] However, most PTEs have been isolated from mesophilic microorganisms and show moderate stability limiting their potential for bioremediation or development of medical countermeasures to face OP poisoning.[26,27] A subfamily of PLL, namely, PLL-A, is composed of enzymes isolated from thermostable and hyperthermostable bacteria or archaea. Special attention has thus been paid to PLL-

Received: February 27, 2024
Revised: April 11, 2024
Accepted: April 12, 2024
Published: April 25, 2024

ACS Publications
© 2024 The Authors. Published by American Chemical Society

https://doi.org/10.1021/jacsau.4c00179
JACS Au 2024, 4, 1941−1953

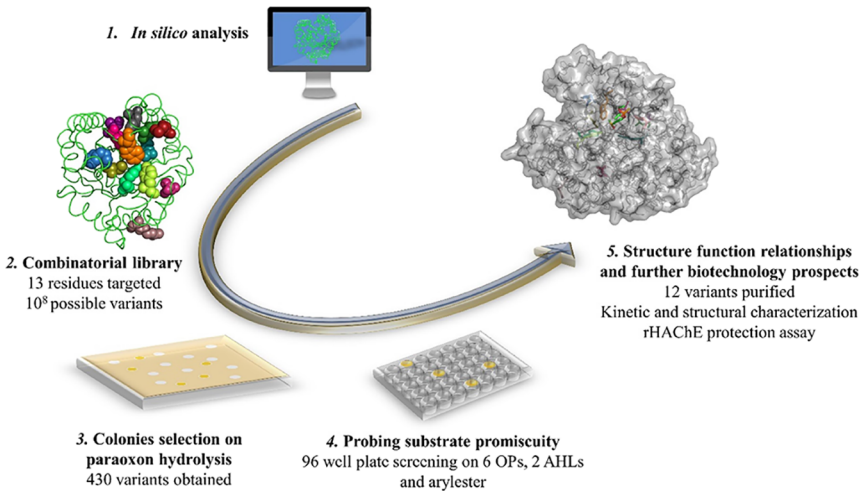

Figure 1. Structure-based design and directed evolution of *Sso*Pox. (1) In silico analyses were performed to compare *Sso*Pox with bacterial PTE from *Brevundimonas diminuta*. (2) 13 residues were targeted for designing a combinatorial library using a degenerated oligonucleotide-based strategy. (3) A solid-based screening was adapted to identify variants retaining a paraoxonase activity. (4) A miniaturized procedure was used to screen a 430-variant library against 9 substrates. (5) Most relevant variants were produced, purified, and characterized for further characterization.

A for developing high-potential biocatalysts as robust enzymes that may offer numerous biotechnological advantages including resistance to high temperatures, tolerance to solvents and denaturants, and long-term storage.[28] Moreover, thermostable enzymes are relevant for directed evolution strategies as their robustness may buffer deleterious mutations and offer new evolutionary trajectories.[29−32] In that context, the enzyme *Sso*Pox isolated from the hyperthermophilic archaeon *Saccharolobus solfataricus* was investigated. *Sso*Pox is a natural lactonase with a promiscuous phosphotriesterase activity toward paraoxon (also referred to as paraoxonase) which has been considered due to its tremendous thermostability (T_m = 106 °C).[33−35] This enzyme and related variants were previously shown to decontaminate a variety of phosphotriesters, such as insecticides, chemical warfare agents, or their surrogates, and could decrease OP poisoning in animal models.[36−42]

Here, we report the redesign of *Sso*Pox's active site using structure-based design and combinatorial strategies to alter its activity and understand the determinants for its activity profile (Figure 1). A combinatorial library was synthesized using degenerated oligonucleotides to diversify 13 positions, and an activity-based screening procedure was used to purge deleterious mutations. The most efficient variants were produced and purified, their catalytic parameters were determined toward 10 substrates (Figure 2), and the melting temperatures were measured. The determination of the tridimensional structures for some of the most improved variants reveals potential structural determinants of the observed transition in catalytic activity.

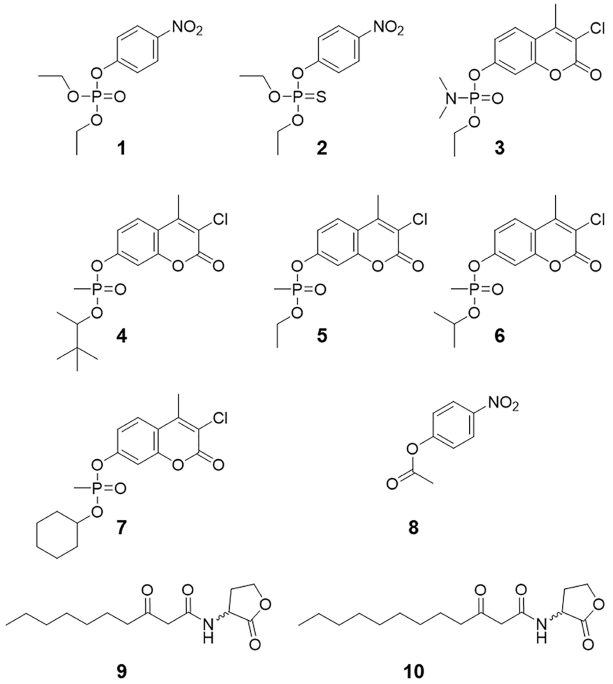

Figure 2. Substrates used in this study. Ethyl-paraoxon (**1**), ethyl-parathion (**2**), tabun analogue (**3**), soman analogue (**4**), VX analogue (**5**), sarin analogue (**6**), cyclosarin analogue (**7**), pNP-acetate (**8**), 3-oxo-C10 AHL (**9**), and 3-oxo-C12 AHL (**10**).

2. MATERIALS AND METHODS

2.1. Chemicals

OP compound analogues were synthesized by Enamine Ltd. All other chemicals used for kinetic assays were ordered from Sigma-Aldrich.

2.2. Screening of the Library

The combinatorial library was synthesized by GenScript (Table S1) and was cloned in a pET32b-Δtrx vector using *NdeI* and *XhoI* restriction sites. The plasmid library was transformed, by electroporation, into the chaperone expressing strain *Escherichia coli* strain BL21(DE_3)-pGro7/GroEL (TaKaRa). Cells were grown overnight at 37 °C on nitrocellulose membranes (Amersham Protran, GE Healthcare) in plates containing ZYP agar medium (supplemented with 100 μg mL^{-1} ampicillin and 34 μg mL^{-1} chloramphenicol). For the induction, nitrocellulose membranes were transferred to ZYP agar medium plates (supplemented with 100 μg mL^{-1} ampicillin and 34 μg mL^{-1} chloramphenicol) containing L-arabinose 0.2% and $CoCl_2$ 0.2 mM. Plates were incubated at room temperature overnight. Cell lysis was realized by thermal shock, with three cycles of 30 s at 37 and −20 °C. For the selection of clones, nitrocellulose membranes were transferred on plates containing ethyl-paraoxon 250 μM, agarose 1.5%, and *activity buffer* (NaCl 150 mM, HEPES 50 mM, $CoCl_2$ 0.2 mM pH 8) (Figure S1). Colonies capable of degrading paraoxon were identified by their yellow color through visual inspection of the plate and were isolated. A total of 430 variants was obtained.

https://doi.org/10.1021/jacsau.4c00179
JACS Au 2024, 4, 1941−1953

Table 1. Catalytic Parameters of Selected *Sso*Pox Variants Against Insecticides, an Ester, and Lactones

substrate	*Sso*Pox	k_{cat} (s^{-1})	K_M (μM)	k_{cat}/K_M (M^{-1} s^{-1})	ratio/*wt*
ethyl-paraoxon	*wt*[a]	$1.26 \pm 0.13 \times 10^{1}$	$2.42 \pm 0.37 \times 10^{4}$	$5.19 \pm 0.95 \times 10^{2}$	1
	IH1	$4.00 \pm 0.30 \times 10^{-2}$	$8.81 \pm 1.41 \times 10^{2}$	$4.38 \pm 2.16 \times 10^{1}$	0.08
	IG7	1.69 ± 0.20	$8.93 \pm 2.12 \times 10^{2}$	$1.89 \pm 0.94 \times 10^{3}$	3.64
	IIIC1[b]	$6.99 \pm 0.25 \times 10^{1}$	$6.10 \pm 0.50 \times 10^{2}$	$1.14 \pm 0.50 \times 10^{5}$	220
	IIIB8	$3.30 \pm 0.20 \times 10^{-1}$	$5.05 \pm 0.68 \times 10^{2}$	$6.47 \pm 2.62 \times 10^{2}$	1.25
	IIIE11	$3.00 \pm 0.20 \times 10^{-2}$	$6.01 \pm 0.91 \times 10^{2}$	$4.47 \pm 1.93 \times 10^{1}$	0.09
	IVE2	$3.30 \pm 0.20 \times 10^{-1}$	$1.19 \pm 0.15 \times 10^{3}$	$2.78 \pm 1.51 \times 10^{2}$	0.54
	IVG2	$2.20 \pm 0.20 \times 10^{-1}$	$1.24 \pm 0.16 \times 10^{3}$	$1.75 \pm 0.96 \times 10^{2}$	0.34
	IVA4	[c]	[c]	$1.06 \pm 0.02 \times 10^{4}$	20.4
	IVE5	[c]	[c]	$1.69 \pm 0.05 \times 10^{3}$	3.26
	IVB10	$3.06 \pm 0.11 \times 10^{2}$	$1.11 \pm 0.78 \times 10^{3}$	$2.75 \pm 1.46 \times 10^{5}$	530
	IVE10	2.81 ± 0.09	$2.04 \pm 0.24 \times 10^{2}$	$1.38 \pm 0.39 \times 10^{4}$	26.6
	VA7	$2.40 \pm 0.10 \times 10^{-1}$	$2.58 \pm 0.39 \times 10^{2}$	$9.17 \pm 2.86 \times 10^{2}$	1.77
	αsD6[d]	$3.22 \pm 0.18 \times 10^{1}$	$1.09 \pm 0.12 \times 10^{3}$	$2.95 \pm 1.55 \times 10^{4}$	56.8
	W263I[a]	[c]	[c]	$1.21 \pm 0.06 \times 10^{3}$	2.33
ethyl-parathion	*wt*[a]	ND[f]	ND	ND	ND
	IH1	ND	ND	ND	ND
	IG7	ND	ND	ND	ND
	IIIC1	$8.20 \pm 0.40 \times 10^{-2}$	$3.49 \pm 0.49 \times 10^{2}$	$2.35 \pm 0.08 \times 10^{2}$	ND
	IIIB8	ND	ND	ND	ND
	IIIE11	ND	ND	ND	ND
	IVE2	$2.20 \pm 0.10 \times 10^{-3}$	$5.10 \pm 0.84 \times 10^{2}$	4.44 ± 1.81	ND
	IVG2	$2.30 \pm 0.09 \times 10^{-3}$	$3.00 \pm 0.35 \times 10^{2}$	7.75 ± 2.57	ND
	IVA4	$4.80 \pm 0.10 \times 10^{-1}$	$3.92 \pm 0.25 \times 10^{2}$	$1.22 \pm 0.45 \times 10^{3}$	ND
	IVE5	ND	ND	ND	ND
	IVB10	$2.86 \pm 0.19 \times 10^{-2}$	$7.37 \pm 0.45 \times 10^{2}$	$3.89 \pm 1.81 \times 10^{1}$	ND
	IVE10	$6.71 \pm 0.08 \times 10^{-3}$	$1.45 \pm 0.17 \times 10^{2}$	$4.63 \pm 1.15 \times 10^{1}$	ND
	VA7	$3.40 \pm 0.08 \times 10^{-3}$	$9.52 \pm 1.04 \times 10^{1}$	$3.63 \pm 0.77 \times 10^{1}$	ND
	αsD6[d]	$7.35 \pm 0.36 \times 10^{-1}$	$5.34 \pm 0.62 \times 10^{2}$	$1.38 \pm 0.57 \times 10^{3}$	ND
	W263I	ND	ND	ND	ND
*p*NP acetate	*wt*[e]	$1.70 \pm 0.07 \times 10^{-1}$	$5.45 \pm 0.35 \times 10^{3}$	$3.12 \pm 0.33 \times 10^{1}$	1
	IH1	$2.13 \pm 0.10 \times 10^{-2}$	$5.80 \pm 0.67 \times 10^{2}$	$3.67 \pm 1.56 \times 10^{1}$	1.18
	IG7	$7.08 \pm 0.99 \times 10^{-1}$	$4.65 \pm 0.84 \times 10^{3}$	$1.52 \pm 1.18 \times 10^{2}$	4.87
	IIIC1	$1.21 \pm 0.29 \times 10^{-2}$	$7.12 \pm 2.03 \times 10^{3}$	1.71 ± 1.41	0.05
	IIIB8	$5.92 \pm 0.17 \times 10^{-2}$	$1.86 \pm 0.09 \times 10^{3}$	$3.18 \pm 1.97 \times 10^{1}$	1.02
	IIIE11	$2.28 \pm 0.07 \times 10^{-2}$	$2.99 \pm 0.28 \times 10^{2}$	$7.64 \pm 2.53 \times 10^{1}$	2.45
	IVE2	$2.70 \pm 0.04 \times 10^{-2}$	$8.70 \pm 0.29 \times 10^{2}$	$3.10 \pm 1.52 \times 10^{1}$	0.99
	IVG2	$4.41 \pm 1.13 \times 10^{-3}$	$3.02 \pm 1.10 \times 10^{3}$	1.46 ± 1.03	0.05
	IVA4	ND	ND	ND	ND
	IVE5	ND	ND	ND	ND
	IVB10	$2.75 \pm 0.29 \times 10^{-2}$	$2.11 \pm 0.36 \times 10^{3}$	$1.31 \pm 0.81 \times 10^{1}$	0.42
	IVE10	$2.11 \pm 0.16 \times 10^{-3}$	$1.63 \pm 0.21 \times 10^{3}$	1.29 ± 0.77	0.04
	VA7	$6.29 \pm 0.16 \times 10^{-2}$	$2.02 \pm 0.08 \times 10^{3}$	$3.11 \pm 1.97 \times 10^{1}$	1.00
	αsD6	[c]	[c]	$1.97 \pm 0.27 \times 10^{1}$	0.63
	W263I	$6.71 \pm 0.27 \times 10^{-3}$	$5.79 \pm 0.55 \times 10^{2}$	$1.16 \pm 0.49 \times 10^{1}$	0.37
3-oxo-C10 AHL	*wt*[a]	4.52 ± 0.10	$1.43 \pm 0.15 \times 10^{2}$	$3.16 \pm 0.33 \times 10^{4}$	1
	IH1	$1.84 \pm 0.03 \times 10^{-2}$	$6.79 \pm 0.91 \times 10^{1}$	$2.71 \pm 0.36 \times 10^{2}$	0.01
	IG7	$2.70 \pm 0.13 \times 10^{-1}$	$2.17 \pm 0.36 \times 10^{2}$	$1.24 \pm 0.54 \times 10^{3}$	0.04
	IIIC1	$5.61 \pm 0.29 \times 10^{-1}$	$5.72 \pm 0.81 \times 10^{2}$	$9.80 \pm 3.58 \times 10^{2}$	0.03
	IIIB8	$1.64 \pm 0.06 \times 10^{-2}$	$3.80 \pm 0.47 \times 10^{2}$	$4.33 \pm 1.39 \times 10^{1}$	0.001
	IIIE11	$1.68 \pm 0.04 \times 10^{-2}$	$6.43 \pm 1.29 \times 10^{1}$	$2.61 \pm 0.34 \times 10^{2}$	0.01
	IVE2	$1.08 \pm 0.03 \times 10^{-2}$	$2.10 \pm 0.26 \times 10^{2}$	$5.14 \pm 1.23 \times 10^{1}$	0.002
	IVG2	ND	ND	ND	ND
	IVA4	ND	ND	ND	ND
	IVE5	ND	ND	ND	ND
	IVB10	$8.88 \pm 0.48 \times 10^{-3}$	$4.19 \pm 0.72 \times 10^{2}$	$2.11 \pm 0.67 \times 10^{1}$	0.001
	IVE10	ND	ND	ND	ND
	VA7	$2.60 \pm 0.10 \times 10^{-2}$	$1.52 \pm 0.30 \times 10^{2}$	$1.71 \pm 0.35 \times 10^{2}$	0.01
	αsD6[d]	ND	ND	ND	ND
	W263I[a]	$6.00 \pm 0.90 \times 10^{-1}$	$1.60 \pm 0.44 \times 10^{3}$	$3.74 \pm 1.17 \times 10^{2}$	0.01
3-oxo-C12 AHL	*wt*[a]	1.01 ± 0.13	$4.56 \pm 1.28 \times 10^{2}$	$2.22 \pm 0.68 \times 10^{3}$	1

https://doi.org/10.1021/jacsau.4c00179
JACS Au 2024, 4, 1941−1953

Table 1. continued

substrate	*Sso*Pox	k_{cat} (s^{-1})	K_M (μM)	k_{cat}/K_M (M^{-1} s^{-1})	ratio/*wt*
	IH1	$4.22 \pm 0.30 \times 10^{-3}$	$1.79 \pm 0.42 \times 10^{2}$	$2.36 \pm 0.72 \times 10^{1}$	0.01
	IG7	$6.63 \pm 0.51 \times 10^{-2}$	$2.74 \pm 0.58 \times 10^{2}$	$2.42 \pm 0.88 \times 10^{2}$	0.11
	IIIC1	2.31 ± 0.89	$2.17 \pm 1.11 \times 10^{3}$	$1.06 \pm 0.80 \times 10^{3}$	0.48
	IIIB8	ND	ND	ND	ND
	IIIE11	$7.46 \pm 0.47 \times 10^{-3}$	$1.27 \pm 0.33 \times 10^{2}$	$5.88 \pm 1.44 \times 10^{1}$	0.03
	IVE2	$5.93 \pm 0.73 \times 10^{-2}$	$7.50 \pm 1.70 \times 10^{2}$	$7.91 \pm 4.29 \times 10^{1}$	0.04
	IVG2	ND	ND	ND	ND
	IVA4	ND	ND	ND	ND
	IVE5	ND	ND	ND	ND
	IVB10	ND	ND	ND	ND
	IVE10	ND	ND	ND	ND
	VA7	ND	ND	ND	ND
	αsD6	$1.65 \pm 0.21 \times 10^{-2}$	$7.78 \pm 2.07 \times 10^{2}$	$2.12 \pm 1.04 \times 10^{1}$	0.01
	W263I[a]	1.80 ± 0.05	$1.78 \pm 0.49 \times 10^{1}$	$1.01 \pm 0.28 \times 10^{5}$	45.5

[a]Data taken from Hiblot et al.[36] [b]Data taken from Pashirova et al.[40] [c]Linear regression or one-phase decay estimation. [d]Date taken from Jacquet et al.[38] [e]Data taken from Hiblot et al.[63] [f]ND, not detected.

The selected variants were then expressed in liquid medium as previously described.[38] Shortly, variants were grown on 96-well plates in LB medium (supplemented with 100 μg mL^{-1} ampicillin and 34 μg mL^{-1} chloramphenicol) overnight at 37 °C. 96-Well plates containing 1 mL of ZYP medium were inoculated. After 5 h of growth at 37 °C, 0.2% L-arabinose and $CoCl_2$ 0.2 mM were added for induction, and cultures were grown overnight at room temperature. Cells were harvested by centrifugation, and lysis was performed in *lysis buffer* (50 mM HEPES pH 8.0, 150 mM NaCl, 0.2 mM $CoCl_2$, 0.25 mg mL^{-1} lysozyme, 0.1 mM PMSF, and 10 μg mL^{-1} DNaseI). Lysates were partially purified by heating at 70 °C for 20 min.

Activity assays were performed on partially purified variants for nine substrates: ethyl-paraoxon and p-nitrophenol acetate (250 μM, 405 nm), tested phosphotriester analogues (10 μM, fluorescence 360/40, 460/40 nm), and 3-oxo-C10 and 3-oxo-C12 HSL (250 μM, 577 nm) (Figure S2). Twelve variants were selected, sequenced by GATC Biotech, and purified.

2.3. Production and Purification of *Sso*Pox Wild-Type and Variants

*Sso*Pox variants were produced in *E. coli* BL21(DE_3)-pGro7/GroEL (TaKaRa) chaperone expressing strain using a pET32b-Δtrx plasmid.[33] Cultures were performed in autoinducible ZYP medium (supplemented with 100 μg mL^{-1} ampicillin and 34 μg mL^{-1} chloramphenicol) For each variant, 1 L of culture was produced in 2 L flasks, 0.5 L of medium per flask, induction took place when $OD_{600\ nm}$ reached a value of 0.8−1. During induction, $CoCl_2$ (final concentration 0.2 mM) and L-arabinose (final concentration 2 g L^{-1}) were added, and the incubation temperature was decreased to 23 °C for 20 h. Cultures were stopped, and cells were harvested by centrifugation (4400 g, 10 °C, 20 min); the pellet was resuspended in *lysis buffer* (50 mM HEPES pH 8.0, 150 mM NaCl, 0.2 mM $CoCl_2$, 0.25 mg mL^{-1} lysozyme, 0.1 mM PMSF, and 10 μg mL^{-1} DNaseI) and stored at −80 °C. Cells were then lysed by sonication (3 × 30 s Qsonica, Q700; Amplitude 45). As a prepurification step, the lysate was heated for 30 min at 70 °C. Cell debris and precipitated host proteins were eliminated by centrifugation (14,000 g, 10 °C, 15 min). *Sso*Pox and its variants were concentrated by ammonium sulfate precipitation (75%) and resuspended in 8 mL of *activity buffer* (50 mM HEPES pH 8.0, 150 mM NaCl, 0.2 mM $CoCl_2$). Ammonium sulfate was eliminated by a desalting column step (HiPrep 26/10 desalting, GE Healthcare; ÄKTA Avant). The sample was concentrated to 2−3 mL for separation on exclusion size chromatography (HiLoad 16/600 Superdex 75pg, GE Healthcare; ÄKTA Avant). Finally, purity was determined by SDS-PAGE, and the protein concentration was measured with a NanoDrop 2000 spectrophotometer (Thermo Scientific).

2.4. Kinetic Assays

2.4.1. Generalities. Catalytic parameters were measured at 25 °C in triplicate in 96-well plates using a reaction volume of 200 μL and recorded by a microplate reader (Synergy HT, BioTek, USA) in a 6.2 mm path length cell and using Gen5.1 software, as previously explained.[33] We note that while the enzyme and its variants are thermostable, this temperature was chosen to produce data that may be relevant to a possible use in bioremediation. Autohydrolysis of the tested substrates was taken into account and subtracted from the enzymatic hydrolysis. In the reaction volume, enzyme concentrations used were between 1×10^{-5} and 1×10^{-8} M depending on the substrate and the variant.

GraphPad Prism 6 software was used to derive catalytic parameters by fitting the data to the *Michaelis−Menten* (MM) equation. When V_{max} could not be reached, catalytic efficiency was determined by fitting the linear part of the MM plot to a linear regression. For phosphotriester analogues, low concentration of substrates was used (10 μM), k_{cat}/K_M were estimated using *one-phase decay* nonlinear regression in GraphPad Prism 6 software. Catalytic parameters are presented in Tables 1 and S2, and all curves used for kinetic analyses are presented in Figures S3 and S4.

2.4.2. Phosphotriesterase Activity Characterization. The kinetic assays were done in *activity buffer* (50 mM HEPES pH 8.0, 150 mM NaCl, and 0.2 mM $CoCl_2$). The conditions used for pesticides were as follows: ethyl-paraoxon, ethyl-parathion, and *p*-nitrophenol acetate hydrolysis took place at 405 nm (ε = 17000 M^{-1} cm^{-1}) within a range of 0.05−2 mM as the substrate concentration, with each solution made from a 100 mM stock solution in ethanol. For phosphotriester analogues, measurements were taken at 10 μM from a 100 mM stock solution in DMSO. We assumed that $K_M \gg [S]$, thus enabling us to estimate k_{cat}/K_M. Hydrolysis was measured by fluorescence (360/40 and 460/40 nm).

2.4.3. Lactonase Activity Characterization. Lactonase kinetics was performed as described previously.[36] Kinetic parameters were determined in *lac buffer* (2.5 mM Bicine pH 8.3, 150 mM NaCl, 0.2 mM $CoCl_2$, 0.25 mM Cresol purple, and 0.5% DMSO) over a concentration range of 0−2 mM for racemic mixtures of 3-oxo-C10 AHLs and 3-oxo-C12 AHLs. Hydrolysis was followed through measurement of the absorbance at 577 nm (ε = 2923 M^{-1} cm^{-1}).

2.5. Production and Partial Purification of rHAChE

As previously reported, recombinant variant of Human AChE (rHAChE) was produced in *E. coli* Origami B cells transformed with pET32-rAChE-3G4 plasmid kindly provided by Moshe Goldsmith from the Weizmann Institute (Rehovot, Israel).[17] Preculture was realized in 2^{x}YT medium (trypton 16 g L^{-1}, yeast extract 10 g L^{-1}, and NaCl 5 g L^{-1}) supplemented with ampicillin (100 μg mL^{-1}) and grown overnight at 37 °C and under stirring. Inoculates were added (1:50

https://doi.org/10.1021/jacsau.4c00179
JACS Au 2024, 4, 1941−1953

dilution) to 3 L of 2xYT medium with ampicillin and grown at 37 °C until the $OD_{600\ nm}$ reached 1. Then, IPTG was added (final concentration of 0.2 mM), and the temperature was changed to 16 °C. Cultures were grown for 24 h. Cells were harvested by centrifugation (4400 g, 4 °C, 20 min), resuspended with 300 mL of *rHAChE lysis buffer* (13 mM Tris pH 8.0, 33 mM NaCl, 10 mM EDTA, 10% glycerol, and 0.25 mg mL^{-1} lysozyme), and stored at −80 °C. Cells were sonicated (3 × 30 s Qsonica, Q700; Amplitude 40). Cell debris were eliminated by centrifugation (14,000 g, 10 °C, 15 min), and 0.1% of octyl glucoside was added. To eliminate more cell debris and host proteins, first ammonium sulfate precipitation was realized, increasing ammonium sulfate concentration from 0 to 40% followed by mixing for 2 h at 4 °C. As previously, centrifugation was done (14000 g, 10 °C, 15 min), and a second ammonium sulfate cut was performed in the supernatant, increasing the concentration of ammonium sulfate from 40 to 50% followed by overnight precipitation of rHAChE at 4 °C. Centrifugation was done (14,000 g, 10 °C, 15 min), and the pellet was resuspended in *rHAChE buffer* (13 mM Tris pH 8.0, 33 mM NaCl, 10 mM EDTA, 10% glycerol) with 0.1% of octyl glucoside. Ammonium sulfate was removed by injection on a desalting column (HiPrep 26/10 desalting, GE Healthcare; ÄKTA Avant). The sample was concentrated before separation on exclusion size chromatography (HiLoad 16/600 Superdex 75pg, GE Healthcare; ÄKTA Avant). The activity of fractions containing partially purified rHAChE was measured using Ellman's reagent (DTNB, 4 mM) and acetylthiocholine (2.5 mM), following the reaction at 412 nm over 10 min.[43] Fractions with activity were gathered and concentrated to reach around 2−3 U mL^{-1}.

2.6. rHAChE Inhibition Assay

Inhibition assays were performed as previously described.[17,44] Briefly, the assay was divided into two steps. First, a reaction mixture containing *Sso*Pox (at 0.1, 1, or 10 μM) and paraoxon (1.5 μM) was started in *activity buffer*, and samples were taken every minute between 0 and 10 min with a final sample at 20 min. The samples were incubated with rHAChE for 15 min. The second step consisted of measuring the remaining activity of rHAChE using Ellman's reagent (DTNB, 4 mM) and acetylthiocholine (2.5 mM) as described above in *activity buffer* supplemented with DTNB 4 mM. The slopes were used to calculate the remaining percentage of rHAChE activity. Curves were fitted with the *one-phase decay* equation using GraphPad Prism 6 software.

2.7. Melting Temperature Determination

Melting temperatures (T_m) were obtained using differential scanning fluorimetry.[45] Experiments were performed on a CFX96 Touch Real-Time PCR Detection System (Bio-Rad). *Sso*Pox variants were used at 1 mg mL^{-1} in *Tris buffer* (50 mM Tris−HCl, pH 7) and with 1X SYPRO orange (Sigma-Aldrich). Denaturation was performed using the FRET channel. Experiments were performed with temperature increasing from 35 °C up to 95 °C (at a rate of 0.5 °C/15 s). For the most thermostable variants, guanidinium chloride or urea was used with a range between 0.5 and 3 M. Data were fitted with *Boltzmann sigmoidal* equation using GraphPad Prism 6 software (San Diego, California USA, www.graphpad.com), and T_m was extrapolated by *linear regression*.

2.8. Crystallization

Crystallization assays were performed as previously described[14] using the hanging drop vapor diffusion method in 24-well VDX plates with a sealant (Hampton Research, California, USA). Different protein:precipitant ratios were tried (1:1; 1:2; and 1:3), and the plate was incubated at 292 K. For all variants, crystals appeared after 3 days in a solution containing 25% (w/v) PEG 8000 and Tris−HCl buffer (pH 8.5). To obtain quality crystals, microseeding was performed. Protein crystals were harvested from a drop, placed in 5 μL of the mother solution, and vortexed for 1 min. Several dilutions of seeds were performed (50, 75, and 100-fold), and 0.1 μL of these solutions were added to drops containing different protein:precipitant ratios. Attempts were made to cocrystallize these variants with diethyl-4-methylbenzylphosphonate, and crystals were produced for the variants IVA4, IG7, and IVB10, but the compound could not be modeled. Two other structures (IVE2, and some monomers of IIIC1) also show residual, unexplained density near the bimetallic center.

2.9. Data Collection and Structure Refinement

Crystals were transferred into a cryoprotectant solution composed of 20% (v/v) glycerol and crystallization solution. Crystals were then flash-cooled in liquid nitrogen. X-ray diffraction data were collected at 100 K using synchrotron radiation at the 23ID-B beamline (APS, Argonne, Argonne, IL, USA). X-ray diffraction data were integrated and scaled with the *XDS* package (Tables S3 and S4).[46] The phases were obtained by performing a molecular replacement with MOLREP or PHASER using the structure of *Sso*Pox-*wt* (PDB ID 2VC5) as a model.[47,48] The models were built with *Coot* and refined using REFMAC,[49,50] PHENIX,[51] or a combination of both. Structures were validated using Molprobity.[52] Structure illustrations were obtained using PyMOL.[53]

2.10. Structural Analysis

Active site cavities were determined using CAVER Analyst 2.0 beta[54] and a 1.4A *probe* and *large probe* 3.00. For IIIC1, these settings resulted in artifactually small multiple cavities. Therefore, calculations were done by allowing a probe to be up to 4.00, and the program chose a max probe of 3.05 for this variant. Average B-factors were calculated using *Baverage* from the CCP4 program suite v.8.0.004.[55] Phenix was used to combine the X-ray data with molecular dynamics and investigate the ensembles of conformations of loops 7 and 8 of the various generated mutants. Ensemble refinement was performed using the default parameters. The modeled phosphate was left in the structures of IG7, IVA4, and IVB10 during the simulation. Because the anion position changed during the simulations, the possible interference with this molecule with the outcome of the simulation was evaluated by removing the anion and performing new ensemble refinement calculations with the unbound models. While these presented results similar to those of simulation with complete models, it led to the loss of the integrity of the bimetallic center during the simulation (variant IVA4). Therefore, simulations-calculated bound phosphate (when modeled) are presented (Supplementary Movies 1−4).[56,57]

3. RESULTS AND DISCUSSION

3.1. Design and Screening of the Combinatorial Library

Structural analysis was conducted by analyzing the superposition of the structures of *Sso*Pox (PDB ID 2VC5) and *Bd*PTE (PDB ID 1DPM) using PyMOL.[53] The PTE from *B. diminuta* was selected as a template for design because of its high proficiency against OPs,[24] its structural similarity to *Sso*Pox,[14] and its ample, pre-existing structural characterization.[24] Structural analysis identified 13 residues that were identified as interacting or possibly interacting with the substrates and involved in defining the binding cleft shape and chemical properties. The positions V27, L72, Y97, Y99, R154, T177, R223, L226, L228, C258, W263, W278, and I280 were selected for diversification. In order to reduce the size of the combinatorial library, structural analysis was conducted to propose mutations for these positions. The goals for this active site redesign were to increase the size of the smaller subsite to accommodate for the bulkier phosphotriester moiety (as compared to a lactone ring; e.g., mutation of V27 into A or G) and to alter/reconfigure the active site loop conformations by diversifying key loop positions (e.g., W263, mutated into all other residues). The full list of the included diversification is in Table S1.

3.2. Combinatorial Library Screening Yields Higher Activity, Highly Promiscuous Mutants

Initial screening of the combinatorial library using an ethyl-paraoxon colored colony assay allowed the identification of 430 active variants (Figure S1). These variants were subsequently subjected to further screenings using nine substrates including OP compounds ethyl-paraoxon (**1**) and previously reported

https://doi.org/10.1021/jacsau.4c00179
JACS Au 2024, 4, 1941−1953

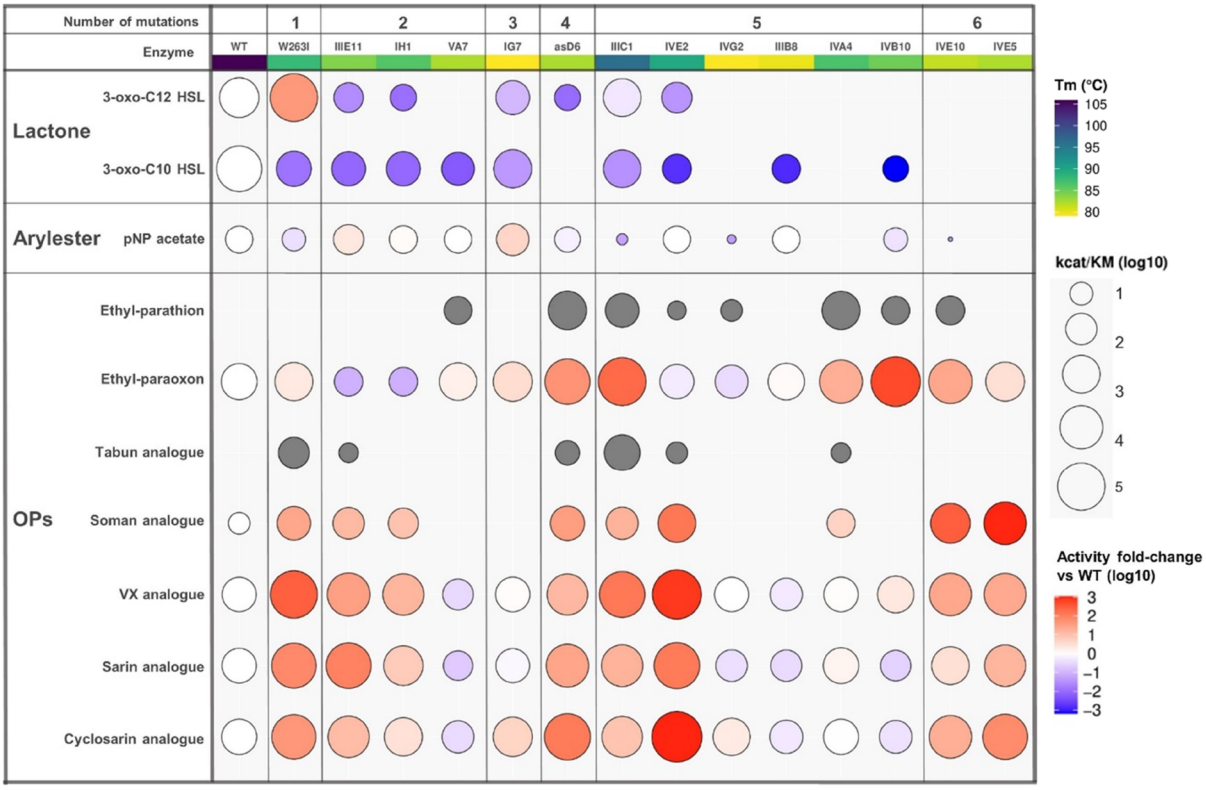

Figure 3. Enzymatic promiscuity and stability profile of *Sso*Pox variants. The heat map shows the selected variants' catalytic efficiency values (circle size) and fold change (fill colors) compared to *Sso*Pox-wt, in logarithmic values. Gray fill indicates no calculated ratio relative to the wild-type due to a lack of measured wild-type activity toward that substrate. Each column represents the data for a different *Sso*Pox variant, while each row shows the results for a different substrate. Variants are organized by the number of combined mutations (top row). The second table row indicates the variant names and their melting temperature (T_m) values (specific values are given in Table S5). The heat map was designed using the ggplot2 package on R.

phosphotriester analogues (**3**−**7**),[56,58] arylester (*para*-nitrophenyl acetate, **8**), and acyl-homoserine lactones (3-oxo-C10 AHL, **9** and 3-oxo-C12 AHL, **10**). The results from these screenings are presented as a heat map in the Supporting Information (Figure S2). From these results, 12 highly active variants were identified and subsequently subjected to complete kinetic characterization toward the nine previously (**1**, **3**−**10**) listed substrates and ethyl-parathion (**2**). The 12 highly active variants harbor 2 to 6 mutations, and the mutations they carry are listed in Table S5. The obtained kinetic parameters can be compared to those of the wild-type enzyme (*Sso*Pox-*wt*) and the two previously reported, improved lactonase and phosphotriesterase variants of *Sso*Pox (*i.e.* W263I and αsD6);[36,38] (Tables 1 and S2, Figures 3, S3, and S4). Data reveal that the variants IIIC1 and IVB10 exhibit 220- and 530-fold increases in catalytic efficiency with ethyl-paraoxon as a substrate as compared to *Sso*Pox-*wt*. Other activity improvements were noted. For example, variant IG7 shows an ∼5-fold increase in catalytic efficiency for arylesterase activity (Table 1). Both arylesterase and phosphotriesterase were improved with a similar magnitude for IG7 compared to *Sso*Pox-*wt*. Interestingly, large improvements of phosphotriesterase and arylesterase activity appear concomitant with a drastic reduction in their lactonase activity (Figure 3). This loss in activity results in large specificity shifts of up to ∼10^6-fold. These activities therefore appear to functionally trade-off in the *Sso*Pox enzyme. Overall, several variants, such as IIIC1 and IVE2, appear significantly more promiscuous than *Sso*Pox-*wt* (Figure 3).

3.3. Improved Variants IIIC1 and IVA4 Do Not Show Any Thiono-effect

Remarkably, most (7 out of 12) characterized variants showed detectable ethyl-parathion activity, while *Sso*Pox-*wt* did not (Table 1). The absence of activity against ethyl-parathion is intriguing because it differs from ethyl-paraoxon only by the substitution of the terminal oxygen atom on the phosphorus atom with the sulfur atom (Figure 2). While this change is chemically very significant, it is a modest steric difference. Therefore, it is likely caused by the difference in the chemical properties of both atoms. This preference was previously referred to as thiono-effect: some PLLs were previously described to show a marked preference for oxono-phosphotriesters,[59] whereas PTEs do not show this pattern.[60] The thiono-effect varies in the different variants: the paraoxonase/parathionase activity level ratio ranges from ∼9 to 7069- fold for variants IVA4 and IVB10, respectively. These results show that some mutations in *Sso*Pox are altering the active site environment in such a way that it eliminates the discrimination between oxygen and a sulfur atom. We note that all variants with measurable ethyl-parathion activity levels contain mutations at positions Y97 and Y99.[38] In particular, Y97 is relatively conserved in metallo-lactonases[12] and was shown in other PLLs to be strongly charge-coupled to the metal cation β.[61,62] Interestingly, these tyrosine residues are not present in PTEs, enzymes that typically show very low thiono-effects. However, the mutation of Y97 or Y99 does not appear to be sufficient to reduce the thiono-effect since some variants (e.g., IIIE11, IH1,

https://doi.org/10.1021/jacsau.4c00179
JACS Au 2024, 4, 1941−1953

IIIB8, and IVE5) containing these mutations show no ethyl-parathion activity (Table 1).

3.4. Some Variants Show Very Large Phosphotriesterase Activity Increase

The 12 selected variants were subjected to further kinetic characterizations against several OP compounds. Specifically, coumaric analogues of sarin, cyclosarin, tabun, soman, and VX were previously described.[64] *Sso*Pox-*wt* exhibits low catalytic efficiency values against VX, sarin, cyclosarin, and soman analogues (k_{cat}/K_M values of 2.74×10^2, 3.00×10^2, 3.93×10^2, and 7.63 M^{-1} s^{-1}, respectively), and no detectable activity against the tabun analogue (Table S2, Figure S4). The new variant IVE2 was found to be the most efficient variant against sarin, cyclosarin, and VX analogues with k_{cat}/K_M values reaching 3.90×10^4, 4.38×10^5, and 2.15×10^5 M^{-1} s^{-1}, respectively (Figure 3, Table S2). This represents considerable improvements over *Sso*Pox-*wt*, specifically 130-, 1114-, and 784-folds. When compared to W263I and αsD6, IVE2 shows higher activity for all tested analogues and is ∼9-fold more active against the cylosarin analogue (Table S2). Other variants are also largely improved: variant IVE5 showed a 1076-fold enhancement compared to *Sso*Pox-*wt* with the soman analogue as a substrate. The variant IIIC1 showed improvement toward all five tested analogues and was the most active variant for the hydrolysis of the tabun analogue (k_{cat}/K_M value of 5.28×10^2 M^{-1} s^{-1}).

Overall, a mutation at the position W263 is present in numerous improved variants against the coumarin analogues, including W263I, αsD6, IVE5, IVB10, IVE10, IIIC1, and IVE2. Other variants show improved phosphotriesterase activity without a mutation at position W263 but contain mutations at both Y97 and Y99 positions, including IVA4, IVE2, IIIE11, and IH1. This may suggest that different strategies are at play to increase the activity: mutating W263 mainly affects the loop 8 conformation[36] and mutations at Y97 and Y99 sites may alter the cavity size, its electrostatic properties, and the potential for interactions with the substrate.

3.5. Evaluating the Ability of Improved Variants to Protect Acetylcholinesterase

The best-identified variants in degrading OP compounds (i.e., IIIC1, IVB10, IG7, IVE10, and IVA4) were subjected to further investigations. Specifically, we adapted a previously reported procedure based on the inhibition of Human AChE[17,44] to evaluate their capacity to protect the enzyme target of OP compounds. We used a previously reported stabilized rHAChE.[17,22] rHAChE inhibition assays were performed with ethyl-paraoxon, although rHAChE inhibition by this substrate is not irreversible. rHAChE activity was measured at different time points to evaluate the rate of detoxification of the phosphotriester by the *Sso*Pox variants. The results show that IIIC1 and IVB10 were the fastest mutants to degrade ethyl-paraoxon and thereby protect rHAChE from inactivation. The two mutants, used at a concentration of 0.1 μM, degraded the phosphotriester in 3 min, whereas *Sso*Pox-*wt*, tested at a 100-fold higher enzyme concentration, required more than 10 min (Figure 4). These results were in accordance with the much higher observed catalytic efficiency values for variants IIIC1 and IVB10. Variant IIIC1 was recently evaluated for *in vivo* detoxification of organophosphate, and results showed it could protect mice from ethyl-paraoxon.[40]

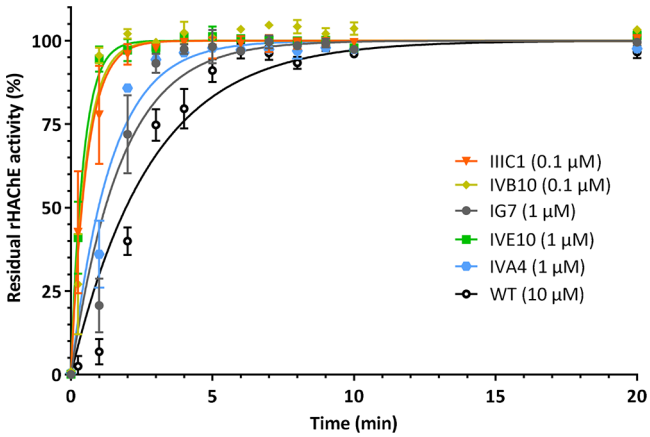

Figure 4. Protection of rHAChE with *Sso*Pox variants. rHAChE activity was evaluated after incubation of paraoxon with *Sso*Pox wild-type and variants (IIIC1, IVB10, IG7, IVE10, and IVA4) at different times. The resulting curves were fitted with a one-phase decay equation using GraphPad Prism 6 software.

3.6. Biochemical Properties of the Improved Variants

The biochemical properties of the obtained mutants, namely, their kinetic properties and their thermal stability, were grouped in a heat map for visualization and analysis (Figure 3). This was performed by compiling a heat map of the overall activities and also by clustering the substrates by type and the variants according to the number and the type of mutations. The melting temperatures were determined for selected variants (Table S5). They show that all variants have reduced thermal stability as compared to *Sso*Pox-*wt*. In fact, the most stable mutant, IIIC1, shows a T_m value of 96.3 °C, a 10 °C reduction from the *Sso*Pox-*wt* T_m value (106 °C). The least stable mutant exhibits a T_m value of 79.1 °C, a nearly 27 °C drop. This is evidence that the identified mutations and/or a combination of mutations are destabilizing. Yet, all mutants remain considerably thermostable, with T_m values above 79 °C (Table S5).

Analysis of the kinetic properties of the variants reveals that while their phosphotriesterase activity was improved, their lactonase activity was greatly decreased. In some variants, some key active site residues are mutated. For example, Y97 and Y99 are mutated in variants IIIE11 and IH1. Y97 in particular was previously reported to be involved in the lactone ring positioning in *Sso*Pox, yet it does not appear required for the lactonase activity.[14] Other observations can be made from the kinetic parameter analysis. It seems that the Y97F mutation is present in mutants with the largest activity increase for ethyl-paraoxon (i.e., IIIC1, IVB10, and IVE10). Previously, the narrowness of the binding cleft in the catalytic subsite of *Sso*Pox-*wt* was highlighted as a factor that prevents the productive binding of the bulkier phosphotriester molecules.[33] The effects induced by the mutation Y97F may be the outcome of a slight reduction of steric hindrance but also suggest that a more apolar environment favors the productive binding of phosphotriesters.

3.7. Selected Mutations Alter the Active Site Loop Conformation and Flexibility

The X-ray structures of some of the most improved variants, namely, IG7, IIIC1, IVA4, IVB10, and IVE2, could be resolved (Table S3). Additional structures for IG7, IVA4, and IVB10 derived from cocrystallization trials with a nonhydrolyzable paraoxon analogue have failed to capture a bound state but allowed the capture of alternative, highly disordered con-

https://doi.org/10.1021/jacsau.4c00179
JACS Au 2024, 4, 1941−1953

formations (Table S4). For some variants, molecules were bound to the active site, as evidenced by the examination of the electron density maps. Because the observed density appeared tetrahedral, a phosphate anion was modeled in the structures of the variants IG7, IVA4, IVB10. Yet, density maps suggest it might correspond to a larger, unidentified molecule (Figure S5 for variant IVB10). The molecules bind onto and between the two metal cations in a similar fashion in all structures and similar to a previous observation made in the structure of another lactonase.[65] The binding of these molecules, modeled as the phosphate anion, does not appear to interfere with the loop conformations in the crystal structures: (i) the observed density is very remote from the loops and (ii) bound and unbound structures are found in both open (e.g., open) and closed (e.g., wt, unbound) conformations (Figure 5).

Overall, the obtained structures are similar to those of *Sso*Pox-*wt*. Indeed, the rmsd on all atoms between *Sso*Pox-*wt* and IVE2, IG7, IIIC1, IVA4, and IVB10 is 0.29, 0.30, 0.29, 0.31, and 0.30 Å, respectively. Interestingly, consistent with observations of previous mutants,[36] most of the changes between the structures occur in loops 7 and 8. This may be due to the localization of the mutations in the protein structure, being mostly situated in the active site vicinity (Figure S6). The largest changes are related to loop 8 conformation (Figure 5). In fact, it appears that there are two groups of loop 8 conformation: a conformation that is similar to that of *Sso*Pox-*wt* that is adopted in the variant IIIC1 (Figure 5), and a second conformation, extended, that is present in the structures of variants αsA6,[38] IVE2, IG7, IVA4, and IVB10 (Figure 5). Interestingly, variant IIIC1 is also the crystallized variant with the highest T_m value (Table S5), and consistently, the thermal B-factor for loops 7 and 8 is lower than those of other variants (Figure 5). With regard to loop 7, the variants show a conformation similar to that of *Sso*Pox-*wt* except for IVB10 (Figure 5).

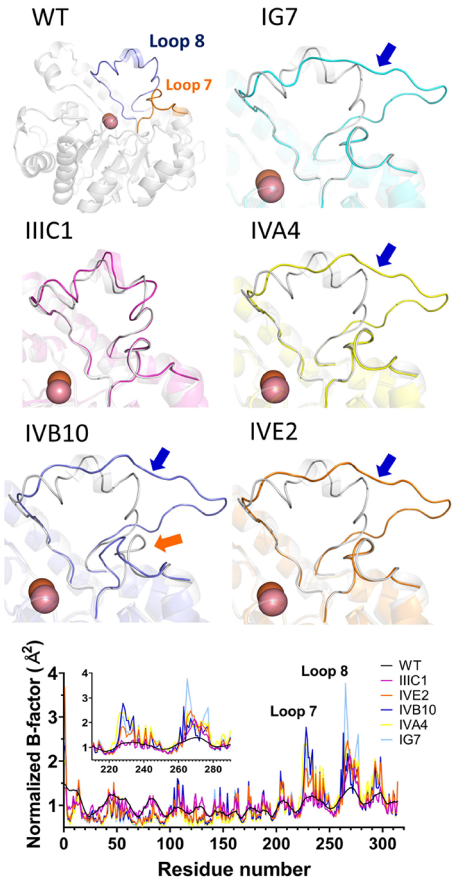

Figure 5. Improved variants show different active site loops 7 and 8 conformations. Active site regions of the variant structures are superimposed with the *Sso*Pox-*wt* structure (light gray; PDB ID 2VC5). The active site location is indicated by the presence of the bimetallic catalytic centers shown as spheres. The *Sso*Pox-*wt* structure and its loops 7 and 8 are highlighted. Significant loop conformation changes are indicated with arrows (blue for loop 8; orange for loop 7). *Bottom graph*: Normalized thermal B-factor values of the different structures are a function of the residue number. A zoomed-in inset for the loops 7 and 8 sequence region is shown. We note that the structures of variants IG7, IVA4, and IVB10 are modeled with a metal-bound phosphate anion, while IIIC1, IVE2, and *Sso*Pox-*wt* are unbound. All structures have a complete bimetallic center.

The active site loops 7 and 8 not only adopt different conformations but also show different conformational flexibilities. The structures highlight that the selected mutations contribute to the increased flexibility of the loops. In fact, for the additional structures solved for the variants IG7, IVA4, and IVB10, much of loops 7 and 8 could not be modeled due to the lack of electronic density, suggesting high levels of disorder (Figure S7). This is confirmed by the alternative structure of variant IG7 that shows low metal occupancy (modeled at 0.5 occupancy) and a possibly partially decarboxylated lysine (KCX137). Similar observations could be made for the alternative structure of variant IVA4, albeit to a lesser extent. The latter structure further illustrates this increased conformational flexibility: it captures nonproductive enzyme conformation caused by loop disorder (Figure S8A). In this conformation, a fragment of loop 8 is bound to the bimetallic active site center and therefore is a nonproductive enzyme conformation (Figure S8B). Residue C258 interacts with the cobalt cation, and C259 forms a disulfide bridge with the mutated position L72C. Other structures reveal partial loop fragments that could be modeled (Figure S7), but the structures show an overall low electronic density to support robust loop modeling. More ordered structures could be obtained for which electron density supported the modeling of discrete loop conformations. Yet, in all these structures, the loop disorder is increased relative to *Sso*Pox-*wt*, with the greatest level of disorder observed in the IVA4 structure (Figure S9). The analysis of the normalized thermal motion B-factor confirms the increased flexibility of loops 7 and 8 (Figures 5 and S10) as compared to *Sso*Pox-*wt* (PDB ID 2VC5). This higher mobility is consistent with the observation that all of the improved variants are destabilized compared to *Sso*Pox-*wt*, as shown by their reduced melting temperature values (Table S5).

The changes in the enzyme's active site for the conformation of loops 7 and 8 lead to a change in the substrate binding cavity size and shape. In fact, all of the variants' structures showed significantly reshaped active site cavities (Figure S11). In addition to the reshaping of the active site due to loop conformation changes, we note that numerous selected mutations include mutations into residues with smaller side chains that increase the volume of the binding cleft in the vicinity of the bimetallic center. This is true for mutations V27G (IG7 and IVA4), V27A (IVB10), Y97F (IIIC1 and IVB10), Y97I (IVA4), Y97L (IVE2), and Y99F (IIIC1, IVA4 and IVB10). This local enlargement around the bimetallic active site center may allow the accommodation of the phosphoester groups that are bulkier than the lactone ring. However, the overall cavity size of the variants did not increase. In fact, each is smaller than that

https://doi.org/10.1021/jacsau.4c00179
JACS Au 2024, 4, 1941−1953

of *Sso*Pox-*wt*, and this is consistent with the observed large decreases in the lactonase activity for these variants because AHL molecules can have very long *N*-acyl chains and may require a larger cavity than phosphotriesters. The cavity volumes are 704.5, 519.0, 523.4, 382.5, 358.8, and 321.6 Å^3 for *Sso*Pox-*wt*, IVA4, IIIC1, IG7, IVB10, and IVE2, respectively. We note that variant IIIC1, with a similar loop conformation to *Sso*Pox-*wt*, retains a larger cavity size and high levels of lactonase activity. Except for variant IVA4, variants with smaller cavities show the lowest lactonase activity levels. These observations suggest that the size of the active site cavity contributes to modulating the activity profile of *Sso*Pox.

3.8. Changes in Interaction Networks and Alteration of the Active Site Loop Conformation

To better understand the molecular determinants for the observed conformational changes, we analyzed the effects of the mutations on the interaction network between the loops and structure core (Figure 6). The analysis of the structure of the variant IG7 suggests a key role for mutation I280T. This residue anchors the C-termini of the active site loop 8 into the protein hydrophobic core. The mutation I280T may decrease this anchorage, and the threonine residue creates new interactions with E52 main and side chains via two discrete conformations. This rearrangement causes the side chain of S279 to interact more closely with the side chain of T281 (3.2 Å in IG7, 3.4 Å in the *Sso*Pox-*wt* structure) and repositions the side chain of E52.

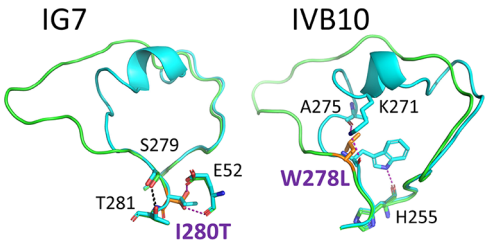

Figure 6. Mutations contribute to active site loop conformational changes. The variant structures (in green) are superposed onto the structure of *Sso*Pox-wt (in cyan). Mutated residues are highlighted in orange. Interactions are shown as dashed lines, and interactions of interest are shown as purple dashed lines.

For some variants, the structure does not immediately reveal a possible mechanism for the altered conformation. For example, variant IIIC1 that also possesses I280T shows very similar features: a new interaction between I280T and E52, and S279 interacting more closely with T281. Yet, in this case, these changes are not sufficient to alter the conformation of loop 8 that adopts a *wt*-like conformation in the resolved IIIC1 structure (Figure S12). Similarly, the mutations present in the IVA4 and IVE2 variants do not show direct connections to the observed conformational changes. For these mutants, alteration of the active site loop conformation may originate from the destabilizing nature of the selected mutations rather than a specific mechanism.

The structure of variant IVB10 suggests that the mutations cause the disruption of an intricate network of hydrogen bonds that exist in the *wt* structure. This disruption results in the more open loop 8 conformation. In the *wt* structure, the side chain of W278 forms a hydrogen bond with the main chain of H255 and interacts with K271 and A275. The mutation at W278L of variant IVB10 completely disrupts this interaction network, and an open-loop conformation is observed (Figure 6).

Other factors are guiding the changes in the loop 8 conformation. In particular, a difference between the variant IG7 and IIIC1 is the nature of the residue in position 263, W (IG7) or V (IIIC1), which was previously shown to affect the loop 8 flexibility and conformation.[36]

3.9. Selected Mutations Modulate Conformational Sampling

Four of the variants' structures could be solved at resolutions at which anisotropic refinement could be performed and resulted in the improvement of the quality of the maps (IG7, IVE2, IVB10, and IVA4). The available high-resolution data confirm the high structural mobility of the loops as illustrated by the corresponding electron density (Figure S9). Examination of the anisotropic atomic displacement parameters of the active site loops 7 and 8 reveals subtle differences between the variants (Figure 7). First, in most cases, the loop disorder appears directional (Figure 7). Interestingly, with some variants, the intensity of the directionality and the direction itself can differ. For instance, variants IG7 and IVE2 exhibit loop 8 with directional anisotropic thermal ellipsoids (particularly IVE2). In contrast, the structures of variants IVB10 and IVA4 exhibit lower degrees of directionality for loops 7 and 8.

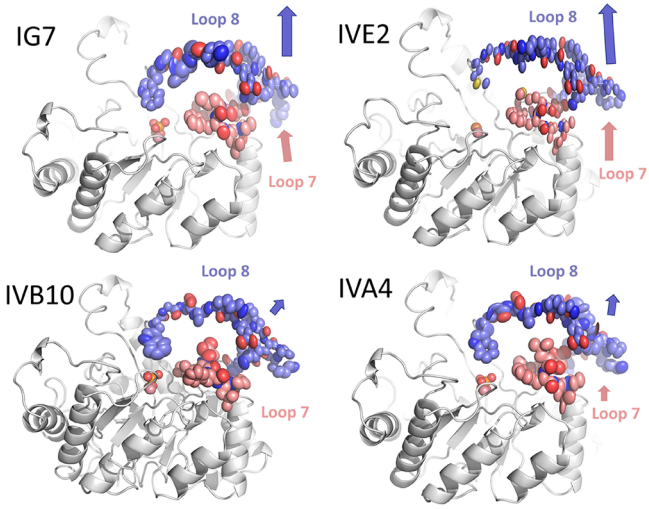

Figure 7. Active site loop conformation and anisotropic thermal B-factor ellipsoids. Arrows are an approximate representation of a major direction and the magnitude of the active site loops' anisotropy. Metal cations and the bound phosphate anion are shown as spheres. The visualization of the ellipsoids was performed by using PyMOL.

The directionality of anisotropic atomic displacement can be indicative of conformational sampling.[66−68] To further investigate the latter, ensemble refinement, that is a combination of X-ray structure refinement and molecular dynamics,[57] was performed to reveal the conformational ensembles of the active site loops. The different analysis results are presented as movies (Supplementary Movies 1−4). The analysis of ensemble conformations confirms the existence of different conformational samplings in the variants. Consistent with the anisotropic displacement, it shows the directionality of loop 8 conformational sampling for variants IG7 and IVE2 (mostly vertical, as shown in Figure 7). Conformational ensembles show a slightly different directionality for loop 8 in variants IVB10 and IVA4 (more horizontal, as shown in Figure 7), although IG7 also exhibits some of this directionality too. Interestingly, the ensemble analysis shows that loop 7 appears substantially

https://doi.org/10.1021/jacsau.4c00179
JACS Au 2024, 4, 1941−1953

more mobile in variants IVB10 and IVA4 as compared to IG7 and IVE2. This is also visible in the analysis of thermal motion B-factors (Figure S10).

Overall, these observations seem to define conformational clusters: despite having adopted a similar conformation, the loop sampling may be different in these different variants. These two clusters are exemplified by the important loop 7 and 8 sampling differences between IVA4 and IVE2, two of the most different variants in their substrate preference profiles (Figure 3). The notion that fine sampling can be captured in the crystal structure has been recently exploited to unravel mechanisms.[69,70] Different conformational clusters were previously described in PTEs[15,68] and hypothesized in *Sso*Pox.[36] Interestingly, these distinct structural clusters also correspond to functional clusters: variants IG7 and IVE2 both show high lactonase and esterase activities, while variants IVB10 and IVA4 show very low lactonase and esterase activities. A previous effort to construct evolutionary intermediates between lactonases and phosphotriesterases showed that the drastic specialization of these enzymes can be done via loop remodeling (i.e., deletion in loop 7).[71] The results presented here suggest that it can also be achieved by altering the active site loop conformational sampling.

The importance of conformational dynamics in enzyme catalysis has been documented but remains a hot topic of discussion.[72−75] Yet, conformational dynamics have emerged as a key player to explain the creation of new enzymatic activities.[15,73] The results presented in this study suggest that conformational changes may be necessary but might not be sufficient for changing an enzyme's activity. This is evidenced by the considerable remodeling of *Sso*Pox's binding cleft, directly caused by the conformational changes of the active site loops 7 and 8. However, while these changes appear important, they may not be sufficient: IIIC1 is a mutant with improved phosphotriesterase activity and shows loop conformations similar to those of *Sso*Pox-wt. Examination of the high-resolution diffraction data and the anisotropic atomic displacement parameters for the active site loops suggest that conformational sampling, and the directionality of the latter is related to the enzyme's activity profile. We surmise that the loop sampling direction could favor or disfavor productive enzyme association with specific substrates. Such possible importance of conformational directionality was previously highlighted in the swiveling motion between its central domain and its nucleotide-binding domain,[76] as well as loop dynamics in adenylate kinase.[77] Such subtle changes constitute an additional informational level beyond the existence of discrete conformations and could improve our understanding of the contributions from distant mutations to catalysis and activity profiles.

4. CONCLUSIONS

In this work, we demonstrated the possibility of redesigning the active site of lactonase *Sso*Pox using structure-based design and combinatorial libraries. Main improvements came at the cost of the initial lactonase activity: some of these variants are now specialized phosphotriesterases. This is in contrast with previous approaches to the evolution of PTEs, where bifunctional enzymes with relatively high proficiency could be obtained using random mutagenesis before significant trade-offs were observed.[78] Here, it may have been mainly caused by changes in the active site loops conformational sampling, and the collected structural data inform us about the active site requirements for both the lactonase and phosphotriesterase activities. The designed mutations and their combinations appear to be destabilizing and considerably reshape the enzyme active site cavity via reorganization of the active site loops. Notably, high-resolution structural data and analysis of the anisotropic atomic displacement parameters suggest that loop conformational sampling and its directionality seem to correlate with the accepted substrates. While these observations may be important to future engineering projects on *Sso*Pox to improve its phosphotriesterase and lactonase activities, they also hint at the possible importance of loop sampling direction in defining enzymes' activity profiles.

■ ASSOCIATED CONTENT

Data Availability Statement

The X-ray structures were deposited to the Protein Data Bank (https://www.rcsb.org/). All remaining data supporting this work are included in the manuscript, the supplementary files and available at the Open Science Foundation at this address: https://osf.io/f4xe6/.

Supporting Information

The Supporting Information is available free of charge at https://pubs.acs.org/doi/10.1021/jacsau.4c00179.

Screening procedure; screening results; kinetic parameters determination; kinetic parameters determination for phosphotriester analogues; protection of rHAChE with SsoPox variants; modeled phosphate anion in the active site of variant IVB10; structural location of mutations; superposition of alternative variants' structures; alternative loop 8 conformation in the second structure of variant IVA4; electron density maps for loops 7 and 8; representation of thermal motion B-factors; active site cavities analysis; variant mutations in the vicinity of loop 8; desired mutations and corresponding codons used to synthesize the variants library; catalytic parameters of SsoPox variants assayed with OP compound analogues; data collection and structure refinement statistics; data collection and structure refinement statistics for alternate, disordered conformations; mutation list of the selected SsoPox variants and their corresponding melting temperature (PDF)

Conformational ensemble for variant IG7 (MPG)

Conformational ensemble for variant IVE2 (MPG)

Conformational ensemble for variant IVB10 (MPG)

Conformational ensemble for variant IVA4 (MPG)

■ AUTHOR INFORMATION

Corresponding Authors

David Daudé − *Gene&GreenTK, Marseille 13005, France*; Phone: 33-626-784-214; Email: david.daude@gene-greentk.com

Mikael H. Elias − *Biotechnology Institute and Department of Biochemistry, Molecular Biology and Biophysics & Biotechnology Institute, University of Minnesota, St. Paul, Minnesota 55108, United States*; orcid.org/0000-0003-0406-7539; Phone: 1-612-626-1915; Email: mhelias@umn.edu

Authors

Pauline Jacquet − *Gene&GreenTK, Marseille 13005, France*

Raphaël Billot − *Gene&GreenTK, Marseille 13005, France*; orcid.org/0009-0002-7461-7890

https://doi.org/10.1021/jacsau.4c00179
JACS Au 2024, 4, 1941−1953

Amir Shimon − *Biotechnology Institute, University of Minnesota, St. Paul, Minnesota 55108, United States*
Nathan Hoekstra − *Biotechnology Institute, University of Minnesota, St. Paul, Minnesota 55108, United States*
Céline Bergonzi − *Gene&GreenTK, Marseille 13005, France; Biotechnology Institute, University of Minnesota, St. Paul, Minnesota 55108, United States;* Present Address: Univ. Grenoble Alpes, CNRS, CEA, IBS, F-38000 Grenoble, France
Anthony Jenks − *Department of Biochemistry, Molecular Biology and Biophysics & Biotechnology Institute, University of Minnesota, St. Paul, Minnesota 55108, United States*
Eric Chabrière − *Gene&GreenTK, Marseille 13005, France; Aix Marseille University, Marseille 13005, France*

Complete contact information is available at:
https://pubs.acs.org/10.1021/jacsau.4c00179

Funding

This work received support from "Investissements d'avenir" program (Méditerranée Infection 10-IAHU-03) of the French Agence Nationale de la Recherche (ANR). P.J. received a PhD fellowship from Direction Générale de l'Armement (DGA). The structural biology work was conducted with support from the MnDrive Initiative, the Biotechnology Institute seed grant program, and a University of Minnesota startup funds (to M.H.E.) and in part by the award no. R35GM133487 (to M.H.E.) by the National Institute of General Medical Sciences. The content is solely the responsibility of the authors and does not necessarily represent the official views of the National Institutes of Health.

Notes

The authors declare the following competing financial interest(s): DD is a shareholder and CEO of Gene&GreenTK. EC is a shareholder and a co-founder of Gene&GreenTK. PJ, RB and EC report receiving personal fees from Gene&GreenTK during the study. MHE, DD and EC have filed the patent EP3941206. MHE and CB have a patent WO2020185861A1. MHE is a co-founder, a former CEO and an equity holder of Gene&GreenTK, a company that holds the license to WO2014167140 A1, FR 3068989 A1, FR 19/02834. MHE received fees from Gene&GreenTK. MHE interests with Gene&GreenTK have been reviewed and managed by the University of Minnesota in accordance with its Conflict-of-Interest policies. The remaining authors declare that the research was conducted in the absence of any commercial or financial relationships that could be construed as a potential conflict of interest.

■ ACKNOWLEDGMENTS

We are very grateful to Dr. Moshe Goldsmith from the Weizmann Institute (Rehovot, Israel) for kindly providing the rHAChE plasmid. We are very grateful to the scientists at the Advanced Photon Source (APS, Argonne, IL, USA) and particularly the beamline scientists and coordinators at 23ID-B for their assistance.

■ REFERENCES

(1) Pandya, C.; Farelli, J. D.; Dunaway-Mariano, D.; Allen, K. N. Enzyme Promiscuity: Engine of Evolutionary Innovation. *J. Biol. Chem.* **2014**, *289* (44), 30229−30236.
(2) O'Brien, P. J.; Herschlag, D. Catalytic Promiscuity and the Evolution of New Enzymatic Activities. *Chem. Biol.* **1999**, *6* (4), R91−R105.
(3) Babtie, A.; Tokuriki, N.; Hollfelder, F. What Makes an Enzyme Promiscuous? *Curr. Opin. Chem. Biol.* **2010**, *14* (2), 200−207.
(4) DePristo, M. A. The Subtle Benefits of Being Promiscuous: Adaptive Evolution Potentiated by Enzyme Promiscuity. *HFSP J.* **2007**, *1* (2), 94−98.
(5) Aharoni, A.; Gaidukov, L.; Khersonsky, O.; Gould, S. M.; Roodveldt, C.; Tawfik, D. S. The "evolvability" of Promiscuous Protein Functions. *Nat. Genet.* **2005**, *37* (1), 73−76.
(6) Amitai, G.; Gaidukov, L.; Adani, R.; Yishay, S.; Yacov, G.; Kushnir, M.; Teitlboim, S.; Lindenbaum, M.; Bel, P.; Khersonsky, O.; Tawfik, D. S.; Meshulam, H. Enhanced Stereoselective Hydrolysis of Toxic Organophosphates by Directly Evolved Variants of Mammalian Serum Paraoxonase. *FEBS J.* **2006**, *273* (9), 1906−1919.
(7) Wroe, R.; Chan, H. S.; Bornberg-Bauer, E. A Structural Model of Latent Evolutionary Potentials Underlying Neutral Networks in Proteins. *HFSP J.* **2007**, *1* (1), 79−87.
(8) Bornscheuer, U. T.; Kazlauskas, R. J. Catalytic Promiscuity in Biocatalysis: Using Old Enzymes to Form New Bonds and Follow New Pathways. *Angew. Chem., Int. Ed.* **2004**, *43* (45), 6032−6040.
(9) Daudé, D.; Vergès, A.; Cambon, E.; Emond, S.; Tranier, S.; André, I.; Remaud-Siméon, M. Neutral Genetic Drift-Based Engineering of a Sucrose-Utilizing Enzyme toward Glycodiversification. *ACS Catal.* **2019**, *9* (2), 1241−1252.
(10) Leveson-Gower, R. B.; Mayer, C.; Roelfes, G. The Importance of Catalytic Promiscuity for Enzyme Design and Evolution. *Nat. Rev. Chem.* **2019**, *3* (12), 687−705.
(11) Afriat, L.; Roodveldt, C.; Manco, G.; Tawfik, D. S. The Latent Promiscuity of Newly Identified Microbial Lactonases Is Linked to a Recently Diverged Phosphotriesterase†. *Biochemistry* **2006**, *45* (46), 13677−13686.
(12) Elias, M.; Tawfik, D. S. Divergence and Convergence in Enzyme Evolution: Parallel Evolution of Paraoxonases from Quorum-Quenching Lactonases. *J. Biol. Chem.* **2012**, *287* (1), 11−20.
(13) Bzdrenga, J.; Hiblot, J.; Gotthard, G.; Champion, C.; Elias, M.; Chabriere, E. SacPox from the Thermoacidophilic Crenarchaeon Sulfolobus Acidocaldarius Is a Proficient Lactonase. *BMC Res. Notes* **2014**, *7*, 333.
(14) Elias, M.; Dupuy, J.; Merone, L.; Mandrich, L.; Porzio, E.; Moniot, S.; Rochu, D.; Lecomte, C.; Rossi, M.; Masson, P.; Manco, G.; Chabriere, E. Structural Basis for Natural Lactonase and Promiscuous Phosphotriesterase Activities. *J. Mol. Biol.* **2008**, *379* (5), 1017−1028.
(15) Campbell, E.; Kaltenbach, M.; Correy, G. J.; Carr, P. D.; Porebski, B. T.; Livingstone, E. K.; Afriat-Jurnou, L.; Buckle, A. M.; Weik, M.; Hollfelder, F.; Tokuriki, N.; Jackson, C. J. The Role of Protein Dynamics in the Evolution of New Enzyme Function. *Nat. Chem. Biol.* **2016**, *12* (11), 944−950.
(16) Naqvi, T.; Warden, A. C.; French, N.; Sugrue, E.; Carr, P. D.; Jackson, C. J.; Scott, C. A 5000-Fold Increase in the Specificity of a Bacterial Phosphotriesterase for Malathion through Combinatorial Active Site Mutagenesis. *PLoS One* **2014**, *9* (4), No. e94177.
(17) Cherny, I.; Greisen, P.; Ashani, Y.; Khare, S. D.; Oberdorfer, G.; Leader, H.; Baker, D.; Tawfik, D. S. Engineering V-Type Nerve Agents Detoxifying Enzymes Using Computationally Focused Libraries. *ACS Chem. Biol.* **2013**, *8* (11), 2394−2403.
(18) Bigley, A. N.; Xu, C.; Henderson, T. J.; Harvey, S. P.; Raushel, F. M. Enzymatic Neutralization of the Chemical Warfare Agent VX: Evolution of Phosphotriesterase for Phosphorothiolate Hydrolysis. *J. Am. Chem. Soc.* **2013**, *135* (28), 10426−10432.
(19) Tsai, P.-C.; Fox, N.; Bigley, A. N.; Harvey, S. P.; Barondeau, D. P.; Raushel, F. M. Enzymes for the Homeland Defense: Optimizing Phosphotriesterase for the Hydrolysis of Organophosphate Nerve Agents. *Biochemistry* **2012**, *51* (32), 6463−6475.
(20) Tsai, P.-C.; Bigley, A.; Li, Y.; Ghanem, E.; Cadieux, C. L.; Kasten, S. A.; Reeves, T. E.; Cerasoli, D. M.; Raushel, F. M. Stereoselective Hydrolysis of Organophosphate Nerve Agents by the Bacterial Phosphotriesterase. *Biochemistry* **2010**, *49* (37), 7978−7987.

(21) Hill, C. M.; Li, W.-S.; Thoden, J. B.; Holden, H. M.; Raushel, F. M. Enhanced Degradation of Chemical Warfare Agents through Molecular Engineering of the Phosphotriesterase Active Site. *J. Am. Chem. Soc.* **2003**, *125* (30), 8990−8991.
(22) Jacquet, P.; Rémy, B.; Bross, R. P. T.; van Grol, M.; Gaucher, F.; Chabrière, E.; de Koning, M. C.; Daudé, D. Enzymatic Decontamination of G-Type, V-Type and Novichok Nerve Agents. *Int. J. Mol. Sci.* **2021**, *22* (15), 8152.
(23) Job, L.; Köhler, A.; Eichinger, A.; Testanera, M.; Escher, B.; Worek, F.; Skerra, A. Structural and Functional Analysis of a Highly Active Designed Phosphotriesterase for the Detoxification of Organophosphate Nerve Agents Reveals an Unpredicted Conformation of the Active Site Loop. *Biochemistry* **2023**, *62* (4), 942−955.
(24) Ghanem, E.; Raushel, F. Detoxification of Organophosphate Nerve Agents by Bacterial Phosphotriesterase. *Toxicol. Appl. Pharmacol.* **2005**, *207* (2), 459−470.
(25) Worek, F.; Seeger, T.; Goldsmith, M.; Ashani, Y.; Leader, H.; Sussman, J. S.; Tawfik, D.; Thiermann, H.; Wille, T. Efficacy of the rePON1Mutant IIG1 to Prevent Cyclosarin Toxicity in Vivo and to Detoxify Structurally Different Nerve Agents in Vitro. *Arch. Toxicol.* **2014**, *88* (6), 1257−1266.
(26) Jacquet, P.; Daudé, D.; Bzdrenga, J.; Masson, P.; Elias, M.; Chabrière, E. Current and Emerging Strategies for Organophosphate Decontamination: Special Focus on Hyperstable Enzymes. *Environ. Sci. Pollut. Res.* **2016**, *23* (9), 8200−8218.
(27) Poirier, L.; Jacquet, P.; Plener, L.; Masson, P.; Daudé, D.; Chabrière, E. Organophosphorus Poisoning in Animals and Enzymatic Antidotes. *Environ. Sci. Pollut. Res.* **2021**, *28*, 25081.
(28) Rémy, B.; Plener, L.; Poirier, L.; Elias, M.; Daudé, D.; Chabrière, E. Harnessing Hyperthermostable Lactonase from Sulfolobus Solfataricus for Biotechnological Applications. *Sci. Rep.* **2016**, *6*, 37780.
(29) Tokuriki, N.; Stricher, F.; Serrano, L.; Tawfik, D. S. How Protein Stability and New Functions Trade Off. *PLOS Comput. Biol.* **2008**, *4* (2), No. e1000002.
(30) Tokuriki, N.; Tawfik, D. S. Stability Effects of Mutations and Protein Evolvability. *Curr. Opin. Struct. Biol.* **2009**, *19* (5), 596−604.
(31) Bloom, J. D.; Labthavikul, S. T.; Otey, C. R.; Arnold, F. H. Protein Stability Promotes Evolvability. *Proc. Natl. Acad. Sci. U. S. A.* **2006**, *103* (15), 5869−5874.
(32) Tokuriki, N.; Tawfik, D. S. Chaperonin Overexpression Promotes Genetic Variation and Enzyme Evolution. *Nature* **2009**, *459* (7247), 668−673.
(33) Hiblot, J.; Gotthard, G.; Chabriere, E.; Elias, M. Characterisation of the Organophosphate Hydrolase Catalytic Activity of Sso Pox. *Sci. Rep.* **2012**, *2* (1), 779.
(34) Vecchio, P.; Elias, M.; Merone, L.; Graziano, G.; Dupuy, J.; Mandrich, L.; Carullo, P.; Fournier, B.; Rochu, D.; Rossi, M.; Masson, P.; Chabriere, E.; Manco, G. Structural Determinants of the High Thermal Stability of SsoPox from the Hyperthermophilic Archaeon Sulfolobus Solfataricus. *Extremophiles* **2009**, *13* (3), 461−470.
(35) Merone, L.; Mandrich, L.; Rossi, M.; Manco, G. A Thermostable Phosphotriesterase from the Archaeon Sulfolobus Solfataricus: Cloning. *Overexpression and Properties. Extremophiles* **2005**, *9* (4), 297−305.
(36) Hiblot, J.; Gotthard, G.; Elias, M.; Chabriere, E. Differential Active Site Loop Conformations Mediate Promiscuous Activities in the Lactonase SsoPox. *PLoS One* **2013**, *8* (9), No. e75272.
(37) Merone, L.; Mandrich, L.; Porzio, E.; Rossi, M.; Müller, S.; Reiter, G.; Worek, F.; Manco, G. Improving the Promiscuous Nerve Agent Hydrolase Activity of a Thermostable Archaeal Lactonase. *Bioresour. Technol.* **2010**, *101* (23), 9204−9212.
(38) Jacquet, P.; Hiblot, J.; Daudé, D.; Bergonzi, C.; Gotthard, G.; Armstrong, N.; Chabrière, E.; Elias, M. Rational Engineering of a Native Hyperthermostable Lactonase into a Broad Spectrum Phosphotriesterase. *Sci. Rep.* **2017**, *7* (1), 16745.
(39) Poirier, L.; Brun, L.; Jacquet, P.; Lepolard, C.; Armstrong, N.; Torre, C.; Daudé, D.; Ghigo, E.; Chabrière, E. Enzymatic Degradation of Organophosphorus Insecticides Decreases Toxicity in Planarians and Enhances Survival. *Sci. Rep.* **2017**, *7* (1), 15194.
(40) Pashirova, T.; Shaihutdinova, Z.; Mansurova, M.; Kazakova, R.; Shambazova, D.; Bogdanov, A.; Tatarinov, D.; Daudé, D.; Jacquet, P.; Chabrière, E.; Masson, P. Enzyme Nanoreactor for In Vivo Detoxification of Organophosphates. *ACS Appl. Mater. Interfaces* **2022**, *14* (17), 19241−19252.
(41) Del Giudice, I.; Coppolecchia, R.; Merone, L.; Porzio, E.; Carusone, T. M.; Mandrich, L.; Worek, F.; Manco, G. An Efficient Thermostable Organophosphate Hydrolase and Its Application in Pesticide Decontamination. *Biotechnol. Bioeng.* **2016**, *113* (4), 724−734.
(42) Suzumoto, Y.; Dym, O.; Roviello, G. N.; Worek, F.; Sussman, J. L.; Manco, G. Structural and Functional Characterization of New SsoPox Variant Points to the Dimer Interface as a Driver for the Increase in Promiscuous Paraoxonase Activity. *Int. J. Mol. Sci.* **2020**, *21* (5), 1683.
(43) Ellman, G. L.; Courtney, K. D.; Andres, V.; Featherstone, R. M. A New and Rapid Colorimetric Determination of Acetylcholinesterase Activity. *Biochem. Pharmacol.* **1961**, *7* (2), 88−95.
(44) Goldsmith, M.; Ashani, Y.; Simo, Y.; Ben-David, M.; Leader, H.; Silman, I.; Sussman, J. L.; Tawfik, D. S. Evolved Stereoselective Hydrolases for Broad-Spectrum G-Type Nerve Agent Detoxification. *Chem. Biol.* **2012**, *19* (4), 456−466.
(45) Geders, T. W.; Gustafson, K.; Finzel, B. C. Use of Differential Scanning Fluorimetry to Optimize the Purification and Crystallization of PLP-Dependent Enzymes. *Acta Crystallograph. Sect. F Struct. Biol. Cryst. Commun.* **2012**, *68* (5), 596−600.
(46) Kabsch, W. Automatic Processing of Rotation Diffraction Data from Crystals of Initially Unknown Symmetry and Cell Constants. *J. Appl. Crystallogr.* **1993**, *26* (6), 795−800.
(47) McCoy, A. J.; Grosse-Kunstleve, R. W.; Adams, P. D.; Winn, M. D.; Storoni, L. C.; Read, R. J. *Phaser* Crystallographic Software. *J. Appl. Crystallogr.* **2007**, *40* (4), 658−674.
(48) Vagin, A.; Teplyakov, A. An Approach to Multi-Copy Search in Molecular Replacement. *Acta Crystallogr. D Biol. Crystallogr.* **2000**, *56* (12), 1622−1624.
(49) Emsley, P.; Cowtan, K. *Coot*: Model-Building Tools for Molecular Graphics. *Acta Crystallogr. D Biol. Crystallogr.* **2004**, *60* (12), 2126−2132.
(50) Murshudov, G. N.; Vagin, A. A.; Dodson, E. J. Refinement of Macromolecular Structures by the Maximum-Likelihood Method. *Acta Crystallogr. D Biol. Crystallogr.* **1997**, *53* (3), 240−255.
(51) Adams, P. D.; Afonine, P. V.; Bunkóczi, G.; Chen, V. B.; Davis, I. W.; Echols, N.; Headd, J. J.; Hung, L.-W.; Kapral, G. J.; Grosse-Kunstleve, R. W.; McCoy, A. J.; Moriarty, N. W.; Oeffner, R.; Read, R. J.; Richardson, D. C.; Richardson, J. S.; Terwilliger, T. C.; Zwart, P. H. PHENIX: A Comprehensive Python-Based System for Macromolecular Structure Solution. *Acta Crystallogr. D Biol. Crystallogr.* **2010**, *66* (2), 213−221.
(52) Williams, C. J.; Headd, J. J.; Moriarty, N. W.; Prisant, M. G.; Videau, L. L.; Deis, L. N.; Verma, V.; Keedy, D. A.; Hintze, B. J.; Chen, V. B.; Jain, S.; Lewis, S. M.; Arendall, W. B., III; Snoeyink, J.; Adams, P. D.; Lovell, S. C.; Richardson, J. S.; Richardson, D. C. MolProbity: More and Better Reference Data for Improved All-Atom Structure Validation. *Protein Sci.* **2018**, *27* (1), 293−315.
(53) DeLano, W. L. *The PyMOL Molecular Graphics System*. Delano Scientific: San Carlos, 2002.
(54) Jurcik, A.; Bednar, D.; Byska, J.; Marques, S. M.; Furmanova, K.; Daniel, L.; Kokkonen, P.; Brezovsky, J.; Strnad, O.; Stourac, J.; Pavelka, A.; Manak, M.; Damborsky, J.; Kozlikova, B. CAVER Analyst 2.0: Analysis and Visualization of Channels and Tunnels in Protein Structures and Molecular Dynamics Trajectories. *Bioinformatics* **2018**, *34* (20), 3586−3588.
(55) Winn, M. D.; Ballard, C. C.; Cowtan, K. D.; Dodson, E. J.; Emsley, P.; Evans, P. R.; Keegan, R. M.; Krissinel, E. B.; Leslie, A. G. W.; McCoy, A.; McNicholas, S. J.; Murshudov, G. N.; Pannu, N. S.; Potterton, E. A.; Powell, H. R.; Read, R. J.; Vagin, A.; Wilson, K. S. Overview of the CCP4 Suite and Current Developments. *Acta Crystallogr. D Biol. Crystallogr.* **2011**, *67* (4), 235−242.

https://doi.org/10.1021/jacsau.4c00179
JACS Au 2024, 4, 1941−1953

(56) Briseno-Roa, L.; Oliynyk, Z.; Timperley, C. M.; Griffiths, A. D.; Fersht, A. R. Highest Paraoxonase Turnover Rate Found in a Bacterial Phosphotriesterase Variant. *Protein Eng. Des. Sel.* **2011**, *24* (1−2), 209−211.
(57) Burnley, B. T.; Afonine, P. V.; Adams, P. D.; Gros, P. Modelling Dynamics in Protein Crystal Structures by Ensemble Refinement. *eLife* **2012**, *1*, No. e00311.
(58) Briseno-Roa, L.; Timperley, C. M.; Griffiths, A. D.; Fersht, A. R. Phosphotriesterase Variants with High Methylphosphonatase Activity and Strong Negative Trade-off against Phosphotriesters. *Protein Eng. Des. Sel.* **2011**, *24* (1−2), 151−159.
(59) Hiblot, J.; Bzdrenga, J.; Champion, C.; Chabriere, E.; Elias, M. Crystal Structure of VmoLac, a Tentative Quorum Quenching Lactonase from the Extremophilic Crenarchaeon Vulcanisaeta Moutnovskia. *Sci. Rep.* **2015**, *5*, 8372.
(60) Jackson, C. J.; Liu, J.-W.; Coote, M. L.; Ollis, D. L. The Effects of Substrate Orientation on the Mechanism of a Phosphotriesterase. *Org. Biomol. Chem.* **2005**, *3* (24), 4343−4350.
(61) Hawwa, R.; Aikens, J.; Turner, R. J.; Santarsiero, B. D.; Mesecar, A. D. Structural Basis for Thermostability Revealed through the Identification and Characterization of a Highly Thermostable Phosphotriesterase-like Lactonase from Geobacillus Stearothermophilus. *Arch. Biochem. Biophys.* **2009**, *488* (2), 109−120.
(62) Xiang, D. F.; Kolb, P.; Fedorov, A. A.; Meier, M. M.; Fedorov, E. V.; Nguyen, T. T.; Sterner, R.; Almo, S. C.; Shoichet, B. K.; Raushel, F. M. Functional Annotation and Three-Dimensional Structure of Dr0930 from Deinococcus Radiodurans: A Close Relative of Phosphotriesterase in the Amidohydrolase Superfamily. *Biochemistry* **2009**, *48* (10), 2237−2247.
(63) Hiblot, J.; Gotthard, G.; Chabriere, E.; Elias, M. Structural and Enzymatic Characterization of the Lactonase SisLac from Sulfolobus Islandicus. *PLoS One* **2012**, *7* (10), No. e47028.
(64) Briseño-Roa, L.; Hill, J.; Notman, S.; Sellers, D.; Smith, A. P.; Timperley, C. M.; Wetherell, J.; Williams, N. H.; Williams, G. R.; Fersht, A. R.; Griffiths, A. D. Analogues with Fluorescent Leaving Groups for Screening and Selection of Enzymes That Efficiently Hydrolyze Organophosphorus Nerve Agents. *J. Med. Chem.* **2006**, *49* (1), 246−255.
(65) Bergonzi, C.; Schwab, M.; Naik, T.; Daudé, D.; Chabrière, E.; Elias, M. Structural and Biochemical Characterization of AaL, a Quorum Quenching Lactonase with Unusual Kinetic Properties. *Sci. Rep.* **2018**, *8* (1), 11262.
(66) Kondrashov, D. A.; Zhang, W.; Aranda, R., IV; Stec, B.; Phillips, G. N., Jr. Sampling of the Native Conformational Ensemble of Myoglobin via Structures in Different Crystalline Environments. *Proteins Struct. Funct. Bioinforma.* **2008**, *70* (2), 353−362.
(67) Godsey, M. H.; Davulcu, O.; Nix, J. C.; Skalicky, J. J.; Brüschweiler, R. P.; Chapman, M. S. The Sampling of Conformational Dynamics in Ambient-Temperature Crystal Structures of Arginine Kinase. *Structure* **2016**, *24* (10), 1658−1667.
(68) Jackson, C. J.; Foo, J.-L.; Tokuriki, N.; Afriat, L.; Carr, P. D.; Kim, H.-K.; Schenk, G.; Tawfik, D. S.; Ollis, D. L. Conformational Sampling, Catalysis, and Evolution of the Bacterial Phosphotriesterase. *Proc. Natl. Acad. Sci. U. S. A.* **2009**, *106* (51), 21631−21636.
(69) Fraser, J. S.; Clarkson, M. W.; Degnan, S. C.; Erion, R.; Kern, D.; Alber, T. Hidden Alternative Structures of Proline Isomerase Essential for Catalysis. *Nature* **2009**, *462* (7273), 669−673.
(70) Fraser, J. S.; Jackson, C. J. Mining Electron Density for Functionally Relevant Protein Polysterism in Crystal Structures. *Cell. Mol. Life Sci.* **2011**, *68* (11), 1829−1841.
(71) Afriat-Jurnou, L.; Jackson, C. J.; Tawfik, D. S. Reconstructing a Missing Link in the Evolution of a Recently Diverged Phosphotriesterase by Active-Site Loop Remodeling. *Biochemistry* **2012**, *51* (31), 6047−6055.
(72) O'Brien, P. J.; Hollfelder, F. Hitting a Moving Target?–Understanding How Conformational Diversity Impacts Enzymatic Catalysis. *Curr. Opin. Chem. Biol.* **2010**, *14* (5), 634−635.
(73) Pabis, A.; Risso, V. A.; Sanchez-Ruiz, J. M.; Kamerlin, S. C. Cooperativity and Flexibility in Enzyme Evolution. *Curr. Opin. Struct. Biol.* **2018**, *48*, 83−92.
(74) Kamerlin, S. C. L.; Warshel, A. At the Dawn of the 21st Century: Is Dynamics the Missing Link for Understanding Enzyme Catalysis? *Proteins Struct. Funct. Bioinforma.* **2010**, *78* (6), 1339−1375.
(75) Kamerlin, S. C. L.; Warshel, A. Reply to Karplus: Conformational Dynamics Have No Role in the Chemical Step. *Proc. Natl. Acad. Sci. U. S. A.* **2010**, *107* (17), E72−E72.
(76) Minges, A.; Ciupka, D.; Winkler, C.; Höppner, A.; Gohlke, H.; Groth, G. Structural Intermediates and Directionality of the Swiveling Motion of Pyruvate Phosphate Dikinase. *Sci. Rep.* **2017**, *7* (1), 45389.
(77) Henzler-Wildman, K. A.; Thai, V.; Lei, M.; Ott, M.; Wolf-Watz, M.; Fenn, T.; Pozharski, E.; Wilson, M. A.; Petsko, G. A.; Karplus, M.; Hübner, C. G.; Kern, D. Intrinsic Motions along an Enzymatic Reaction Trajectory. *Nature* **2007**, *450* (7171), 838−844.
(78) Tokuriki, N.; Jackson, C. J.; Afriat-Jurnou, L.; Wyganowski, K. T.; Tang, R.; Tawfik, D. S. Diminishing Returns and Tradeoffs Constrain the Laboratory Optimization of an Enzyme. *Nat. Commun.* **2012**, *3*, 1257.

https://doi.org/10.1021/jacsau.4c00179
JACS Au 2024, 4, 1941−1953